

Review

Morphology-Controlled Nitrogen-Containing Polymers as Synthetic Precursors for Electrochemical Oxygen Reduction Fe/N/C Cathode Catalysts

Yuta Nabae 

Department of Materials Science and Engineering, Tokyo Institute of Technology, 2-12-1 S8-26, Ookayama, Meguro-ku, Tokyo 152-8552, Japan; nabae.y.aa@m.titech.ac.jp; Tel.: +81-3-5734-2429

Received: 2 July 2018; Accepted: 6 August 2018; Published: 8 August 2018



Abstract: Nitrogen-containing aromatic polymers such as polyimide are known for their high thermal stability. While they have been widely used in industry, their relevance to catalysis is still quite limited. In recent years, nitrogen-containing polymers have been explored as precursors of nitrogen-doped carbonaceous materials, which are particularly attractive as non-precious metal catalysts for oxygen reduction in fuel cells. The high thermal stability of nitrogen-containing polymers contributes to an effective control over the morphology of the resulting carbonaceous catalysts. This review article provides an overview of the recent progress on the research and development of Fe/N/C oxygen reduction catalysts prepared from morphology-controlled nitrogen-containing polymers.

Keywords: polyimide; nitrogen-doped carbon; fuel cell; non-precious-metal; mesoporous carbon; rotating ring-disk electrode voltammetry; electrocatalysis; self-assembly; block copolymer

1. Introduction

The electrochemical oxygen reduction reaction (ORR) is very important in view of the principles of green and sustainable chemistry. The four-electron reduction pathway to form H_2O releases a relatively large free energy (1.23 V vs. reversible hydrogen electrode (RHE)) and is an important reaction for fuel cell applications. The two-electron reduction pathway to form H_2O_2 at a lower potential (0.7 V vs. RHE) is also an important reaction with regard to the electrochemical synthesis of H_2O_2 [1–3]. For both reaction pathways, non-precious metal (NPM) catalysts are desired, considering the cost and scarcity of precious metals. The catalysts obtained by pyrolyzing Fe, N, and C-containing precursors have been widely studied, while oxide-based catalysts also constitute another class of NPM catalysts [4–6]. This review article describes an effective approach to obtain a highly active Fe/N/C catalyst.

The history of the development of NPM ORR catalysts began with the discovery of the catalytic activity of Co phthalocyanine for ORR by Jasinski et al. [7]. Chemists were inspired by the similarity of such macrocyclic compounds to natural enzymes and many macrocyclic compounds were subsequently studied as ORR catalysts [8]; however, their catalytic activity and durability were not sufficient to consider their commercialization as fuel cell catalysts. In this context, since Jahnke et al. reported that heat treatment can improve the ORR catalytic activity and durability of macrocyclic compounds [9], numerous attempts were made to develop NPM cathode catalysts by pyrolyzing precursors containing transition metals (mainly Fe or Co), as well as nitrogen and carbon sources [10,11]. In brief, when Fe, N, and C-containing precursors are pyrolyzed at 600–1000 °C, the obtained Fe/N/C catalysts show ORR catalysis to some degree; however, the nature of the catalytic activity depends on the precursors and pyrolysis protocol.

This review article focuses on nitrogen-containing aromatic polymers as precursors of NPM ORR catalysts. To perform effective catalytic reactions, it is desirable that the catalyst possesses a

large surface area. In addition, the catalyst materials in polymer electrolyte fuel cells (PEFCs) must be in contact with the ionomer to promote the proton conductivity of the catalyst layer. Therefore, the catalyst should preferably be in a fine powder state to increase the interfacial area between the catalyst and ionomer. Nitrogen-containing aromatic polymers such as polyimides contain a sufficient amount of nitrogen atoms and have high thermal stability. While the nitrogen atoms can be converted into catalytically active sites in a facile manner, infusible character is desired to control the morphology of the resulting carbonaceous catalysts. This is made possible because the morphology of the polymer can be controlled at the polymerization stage and the high thermal stability contributes to the retention of the morphology during the high temperature carbonization procedure. In the first half of this review, the synthesis of high performance NPM fuel cell catalysts from spherical polyimides is described. The second half describes the formation of mesoporous structures upon pyrolysis of nitrogen-containing polymers, the morphology of which is controlled via the soft-template approach.

2. ORR Reaction Scheme and Active Sites over NPM Catalysts

The structure of the catalytically active sites in such NPM catalysts is still hotly debated. Figure 1 shows the most commonly proposed active sites in ORR catalysts. One particularly convincing model involves a catalytic center based on metal-N coordination, which was proposed based on experimental evidence from time-of-flight secondary ion mass spectrometry (TOF-SIMS), high-angle annular dark field scanning transmission electron microscopy (HAADF-STEM), and extended X-ray absorption fine structure (EXAFS) [12–14]. Simultaneously, metal-free N-doped carbon species with pyridinic and graphitic nitrogen have also been suggested to be responsible for the observed ORR activity based on experimental [15–17] and theoretical studies [18–20].

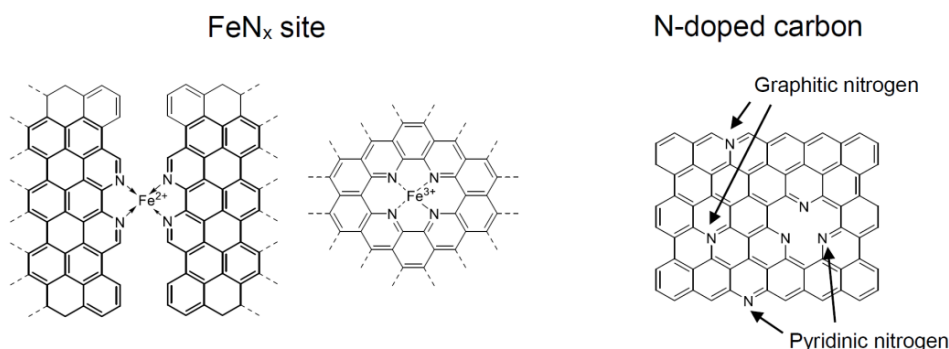


Figure 1. Commonly proposed catalytically active sites for the electrochemical oxygen reduction reaction (ORR) in acidic media.

The difficulties encountered in determining the catalytically active sites arise from the complicated reaction scheme for ORR over Pt-free catalysts. Figure 2a shows a typical reaction model for ORRs [21]. Typical analyses of the Fe/N/C catalysts, including rotating disk electrode (RDE) voltammetry with Koutecky–Levich (KL) and rotating ring-disk electrode (RRDE) voltammetry, tend to exhibit relatively high electron numbers (close to four) [22–24]. However, these analyses cannot resolve the quasi-four-electron reduction, and the experimental data does not support an actual four-electron pathway during NPM catalysis. Indeed, Olson et al. proposed a bi-functional ORR mechanism over Fe/N/C catalysts in 2010 [25], but quantitative discussion to resolve the quasi-four-electron reduction reaction proved difficult. While Ohsaka and co-workers tried to apply the Damjanovic–Hsueh approach [21,26], which involves detailed RRDE analysis by plotting of the obtained parameters against the rotation speeds, such analysis relying on rotation speeds suffered from huge noise [27,28]. To address these concerns, Nabae and co-workers recently developed a new model (Figure 2b) and method for RRDE analysis [29]. This new method avoids overestimating the contribution of the four-electron reduction reaction by studying the different loading densities of the catalysts and

extrapolating the obtained parameters to null loading density. By this analysis, it was revealed that the contribution of the four-electron (I_1) pathway using an Fe/N/C catalyst was only 51% while the rest of the current originated from either of the two two-electron pathways (I_2 and I_3). Note that this correction was done by changing the loading density of the catalyst. Therefore, this extrapolation cannot resolve the 2 + 2 electron pathway proceeding in the inside of the catalyst pores. The inherent contribution from the 2 + 2 electron pathway could be even higher if one considers the reactions in small pores. In this context, as shown in Figure 3, a hybrid mechanism is worth considering for the ORR conducted over Fe/N/C catalysts, where the first two-electron reduction to form H_2O_2 is catalyzed by metal-free N/C catalytic centers and the following two-electron reduction of H_2O_2 and/or the direct four-electron reduction of O_2 to form H_2O are catalyzed by Fe/N/C-based catalytic centers.

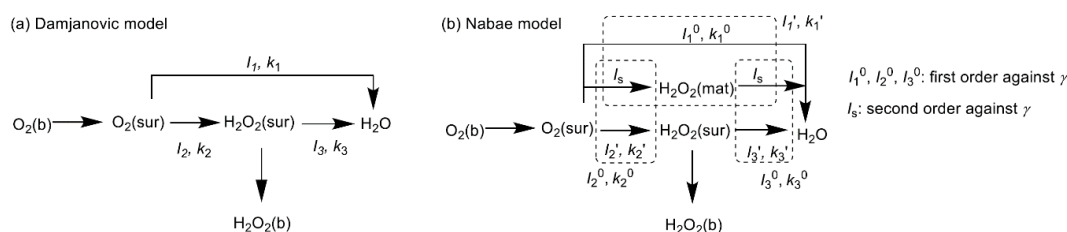


Figure 2. (a) Damjanovic model, which considers only H_2O_2 on the disk electrode surface, H_2O_2 (surf), and (b) Nabae model, which considers H_2O_2 to be further reduced to H_2O in the catalyst layer matrix, H_2O_2 (mat), for the analysis of rotating ring-disk electrode (RRDE) voltammograms of the ORR. I_s refers to the current obtained via the series reaction in the catalyst layer matrix and γ is the catalyst loading density [29].

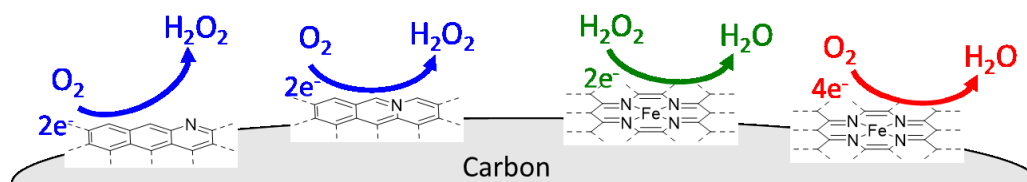


Figure 3. Hybrid mechanism for ORR over Fe/N/C catalysts.

3. Pioneering Studies on Nitrogen-Containing Polymers as Precursors of NPM Catalysts

Since the first report by Jahnke on the pyrolysis of a macrocycle complex [9], the majority of Fe/N/C catalysts have been synthesized by pyrolyzing MN_4 -type macrocycle complexes such as porphyrins and phthalocyanines [30–33]. On the other hand, Dodelet and co-workers proposed that the metal-nitrogen coordination is not essential at the precursor stage, while these authors presented the idea that the metal-nitrogen coordination is finally formed after pyrolysis and responsible for the catalytic activity [34,35]. Based on this rationale, the same research group used polyacrylonitrile as the precursor of Fe/N/C catalysts [36], while focusing on the mechanistic aspect rather than the fabrication of high performance catalysts. There are several recent examples of nitrogen-containing polymers such as polyamide [37], polyaniline [38], and poly(nitroaniline) [39], that have been utilized as the precursors of Fe/N/C catalysts, although none of these studies have paid much attention to the morphology of the nitrogen-containing polymers. The advantages associated with using nitrogen-containing polymers for controlling catalyst morphology have been studied in detail by our research group and are discussed in the next section.

4. Fe/N/C Catalysts Prepared by Pyrolyzing Spherical Polyimides

4.1. Synthesis of Polyimide Nano-Particles

This section focuses on the studies conducted by our research group on polyimide nanoparticles as a precursor for Fe/N/C cathode catalysts. The polymerization technique used for these studies can be classified into the category of precipitation polymerization, which involves a homogenous system where the monomer is completely soluble and present in the continuous phase while the polymer is insoluble and precipitates upon formation [40–43]. Figure 4a shows the synthetic scheme of polyimide nanoparticles from common polyimide precursors, namely, pyromellitic acid dianhydride (PMDA) and 4,4'-oxidianiline (ODA) [44]. As shown in Figures 5 and 6, the particle size can be controlled by changing the temperature and monomer concentration during polymerization. The smallest particle size obtained using the combination of PMDA and ODA was 100 nm (Figure 7a). Polyimide nanoparticles of an even smaller size (60 nm, Figure 7b–d) could be synthesized by adding a dispersant, *N,N*-dimethyldodecylamine, during polymerization. However, the compact particle size was not retained during heat treatment for carbonization in polyimides that were prepared from PMDA and ODA. This was probably because the low molecular weight of the polyimide led to decreased thermal stability, resulting in the fusion of polyimide nanoparticles. To address this concern, ODA was replaced with a tri-amine monomer, 1,3,5-tris(4-aminophenyl) benzene (TAPB), to afford higher thermal stability via cross-linking (Figure 4b) [45]. Fe(acac)₃ was chosen as the Fe source for the above-mentioned polyimide nanoparticles because of its solubility in organic solvents. To afford more uniform and reliable immobilization of the Fe species at the polyimide stage, the copolymerization of a Fe-phenanthroline complex, tris(5-amino-1,10-phenanthroline) iron(II) (Fe(amph)₃²⁺), with PMDA and TAPB was also studied, as shown in Figure 4c [46]. As mentioned later, while this uniform dispersion of the Fe species did not drastically improve the catalytic activity of the resulting carbon, this technique could be important in a scaled-up process because a large-scale production of the precursor would likely suffer from uniformity of chemical composition.

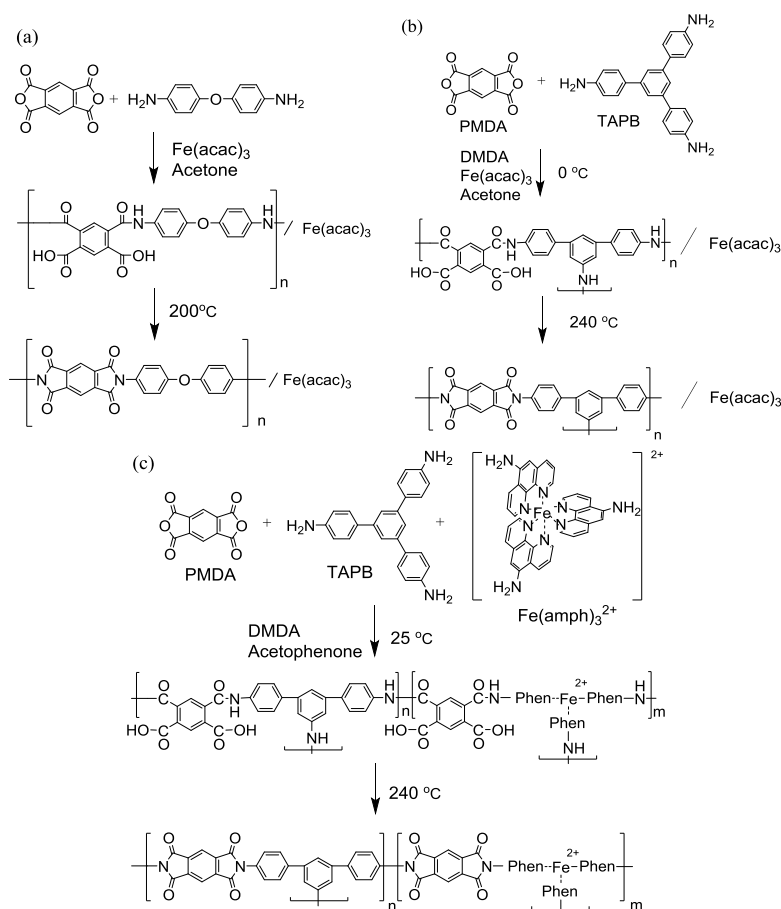


Figure 4. Synthetic routes of polyimide nano-particles of different sizes from (a) pyromellitic acid dianhydride (PMDA) and 4,4'-oxydianiline (ODA) (100–300 nm diameter); (b) PMDA and 1,3,5-tris(4-aminophenyl) benzene (TAPB) in the presence of a surfactant (60 nm diameter); and (c) PMDA, TAPB, and $\text{Fe}(\text{amph})_3$ (uniform dispersion of Fe additive).

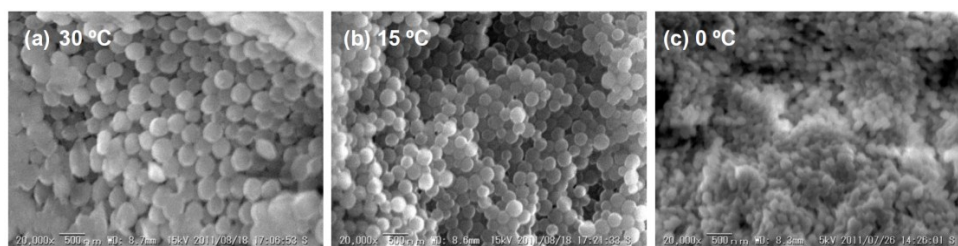


Figure 5. Effect of the polymerization temperature on the morphology of polyimide nano-particles [44].

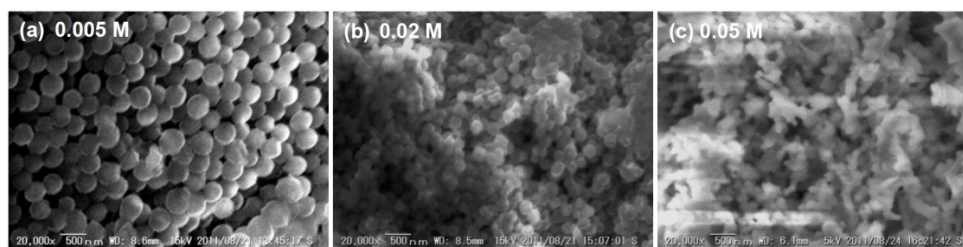


Figure 6. Effect of the monomer concentration on the morphology of polyimide nano-particles [44].

4.2. Fe/N/C Catalysts after the Carbonization of Polyimide Nano-Particles.

The polyimide nanoparticles mentioned above were carbonized to obtain Fe/N/C catalysts by following the protocols listed in Table 1. The FE-SEM images of the samples after carbonization are shown in Figure 7e–h. The first pyrolysis step (the first and second entries) involved 5 h of heat treatment under N₂ atmosphere at 600 °C, followed by acid washing (aw) with HCl (600-N₂-aw). The original chemical structure was almost decomposed and the majority of Fe species were clustered in metallic iron or iron carbide forms [47]. A typical second pyrolysis step was 1 h of heat treatment under NH₃ atmosphere at 800 °C, followed by washing with HCl (800-NH₃-aw). The ammonia treatment effectively increased the surface area of the resulting carbon (i.e., activation) by decomposing the amorphous carbon species. The acid washing process in the first and second steps was essential to retain a meaningful concentration of nitrogen-containing active centers, because extraordinary amounts of Fe nanoparticles catalyze the decomposition and elimination of nitrogen species. The final pyrolysis step involved 1 h of heat treatment under NH₃ atmosphere at 1000 °C. The activation effect at 1000 °C was quite strong and the resulting carbon materials possessed a very high specific surface area (>1300 m² g⁻¹). The pyrolysis protocol described in the third and fourth entries is a modification to avoid the redundant HCl treatment without losing the catalytic activity. To avoid extraordinary amounts of Fe species during carbonization, pyrolysis was started using a lower amount of Fe. In this condition, the Fe-catalyzed carbonization was not as effective as the protocol with 2 wt % of Fe species; therefore, the temperature for the first pyrolysis step was raised to 900 °C (900-N₂) to enhance the degree of carbonization. Subsequently, NH₃ treatments were performed at 800 and 1000 °C without the HCl treatments (800-NH₃ and 1000-NH₃, respectively). The catalysts thus obtained showed similar N and Fe contents and specific surface areas.

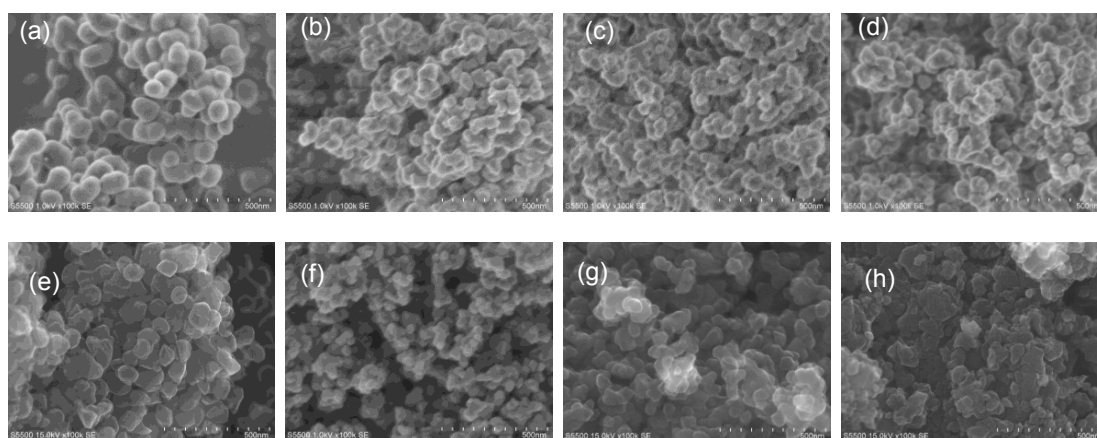


Figure 7. Field emission scanning electron microscopy (FE-SEM) images of polyimide nano-particles and Fe/N/C catalysts after carbonization. (a–d) are the images of polyimide samples obtained by following protocols summarized as Entry 1, 2, 3, and 4 in Table 1, respectively. (e–h) are the images of samples after the carbonization of samples (a–d), respectively.

Figure 8 shows the RRDE voltammograms for the four catalysts described in Table 1. All catalysts showed good ORR catalytic activities. They showed identical ORR currents in the onset region, suggesting that the inherent catalytic activities of these catalysts were quite similar. In contrast, the diffusion limiting currents were slightly different. The catalysts with smaller particles showed higher diffusion limiting currents, probably reflecting the enhanced oxygen diffusion in the catalyst layer matrix. The effect of the particle size on fuel cell characteristics is discussed in the next section.

Table 1. Details of the catalysts prepared with various precursors and protocols.

Catalyst [Ref.]	PI Source	Fe Source	Protocol	Composition (wt %)				BET ³ Surface Area (m ² /g)
				C ¹	H ¹	N ¹	Fe ²	
Fe(2.0)/PI(100) [44]	PMDA ⁴ ODA ⁵	Fe(acac) ₃ 2 wt %	1. 600-N ₂ -aw 2. 800-NH ₃ -aw 3. 1000-NH ₃	90.6	trace	3.1	1.1	1050
Fe(2.0)/PI(60) [45]	PMDA TAPB ⁶	Fe(acac) ₃ 2 wt %	1. 600-N ₂ -aw 2. 800-NH ₃ -aw 3. 1000-NH ₃	90.9	trace	2.8	2.0	1300
Fe(0.3)/PI(60) [46]	PMDA TAPB	Fe(acac) ₃ 0.3 wt %	1. 900-N ₂ 2. 800-NH ₃ 3. 1000-NH ₃	85.5	0.2	2.2	1.0	1380
Fe(0.3)(amph)/PI(60) [46]	PMDA TAPB	Fe(amph) ₃ ²⁺ 0.3 wt %	1. 900-N ₂ 2. 800-NH ₃ 3. 1000-NH ₃	91.0	trace	3.3	0.8	1390

¹ Determined by CHN elemental analysis; ² Determined by electron probe micro analysis (EPMA);

³ Determined by the Brunauer–Emmett–Teller (BET) method; ⁴ Pyromellitic acid dianhydride; ⁵ 4,4'-Oxidianiline;

⁶ 1,3,5-Tris(4-aminophenyl) benzene.

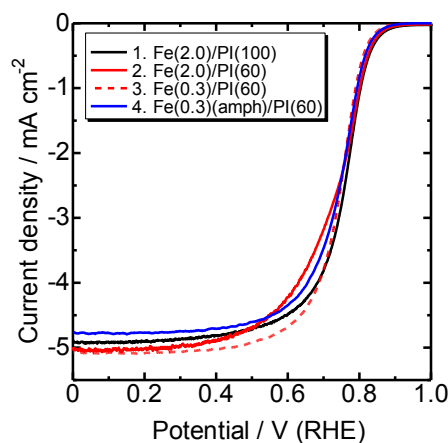


Figure 8. RRDE voltammograms for the samples described as Entry 1, 2, 3, and 4 in Table 1. The individual voltammograms have been reported elsewhere [44–46] and combined in this figure by the author. Temperature: RT, catalyst loading: 0.2 mg cm⁻², electrolyte: O₂ saturated 0.5 M H₂SO₄, rotation: 1600 rpm.

4.3. Fuel Cell Performance

Some of the above-mentioned Fe/N/C catalysts, Fe(2.0)/PI(60) and Fe(2.0)/PI(100), were tested under practical fuel cell conditions. The FE-SEM cross sectional images of the membrane electrode assembly (MEA) are shown in Figure 9. The Fe/N/C catalyst (4 mg) was applied onto the cathode side with a Nafion binder, which resulted in a cathode layer with a thickness of approximately 60 μm . The enlarged images in Figure 9 clearly demonstrate a quite porous and uniform catalyst layer. This ideal morphology could contribute to the successful mass transport diffusion in the catalyst layer.

Figure 10a shows the *I*-*V* performance curves for the MEA prepared using Fe/N/C cathode catalysts. The MEA with the 100 nm cathode catalyst had open circuit voltages of 0.96 and 0.90 V under pure O₂ and air, respectively, and the current density reached 1 A cm⁻² at 0.57 V (O₂) and 0.32 V (air). The MEA with the 60 nm cathode showed similar open circuit voltages of 0.94 V (O₂) and 0.90 V (air) but higher voltages of 0.62 V (O₂) and 0.46 V (air) at a current density of 1 A cm⁻². The better performance with the cathode catalyst having 60 nm particle size probably derives from the enhanced oxygen diffusion in the catalyst layer owing to its well-constructed fine architecture. The performance of the polyimide-derived Fe/N/C catalyst under air was comparable or even better than that of any of the state-of-the-art technologies [48–50]. The durability of the MEAs was investigated by operating the cells over long periods. Figure 10b shows the changes in the cell voltage during operation at 0.2 A

cm^{-2} for 600 h. Although the cell voltage certainly decreased, the cells operated successfully for 600 h. While most of the reported NPM catalysts degrade significantly within 100 h under practical fuel cell conditions, the durability demonstrated in Figure 10 is quite promising. Interestingly, the durability attained by using the 60 nm-catalyst was better than that with the 100 nm-catalyst. As H_2O_2 is known to cause a serious degradation of MEA, this result could be relevant to the 2 + 2 electron ORR mechanism because the fine morphology would contribute to decreasing the concentration of H_2O_2 by the quasi-four electron reduction.

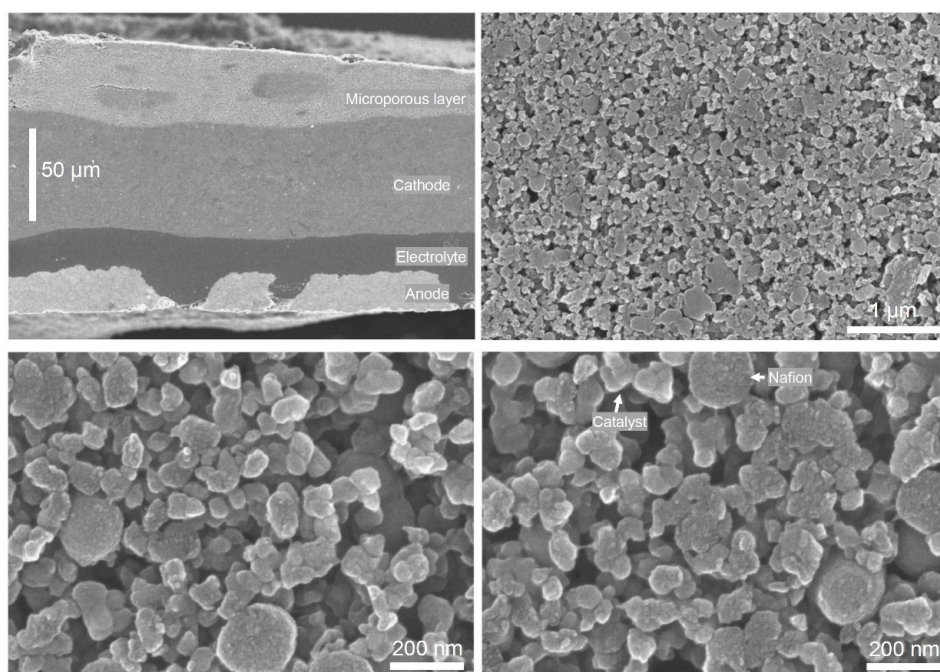


Figure 9. Cross-sectional scanning electron microscopy (SEM) image of the membrane electrode assembly (MEA) with the Fe(2.0)/PI(60) cathode catalyst.

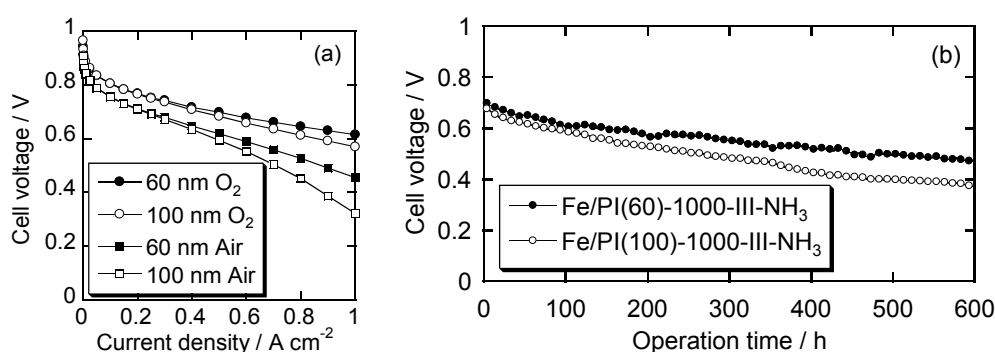


Figure 10. (a) I-V polarization curves under 0.2 MPa of total pressure with the Fe(2.0)/PI(100) and Fe(2.0)/PI(60) catalysts and (b) cell voltage stability curves under 0.2 MPa of air at 0.2 A cm^{-2} . Anode: PtRu/C catalyst with $0.4 \text{ mg-PtRu cm}^{-2}$ loading, humidified H_2 at 80°C . Cathode: 4 mg cm^{-2} catalyst loading, pure or balanced O_2 (humidified) at 80°C . Electrolyte: Nafion NR211. $T = 80^\circ\text{C}$ [45].

5. Mesoporous Fe/N/C Catalysts for Enhanced Oxygen Diffusion

In addition to the above-mentioned strategy of morphological control to obtain spherical particles, the fabrication of mesoporous Fe/N/C catalysts is of considerable interest. Nitrogen-doped mesoporous carbons have been typically synthesized via hard-template approaches [2,51–53]. A mesoporous Fe/N/C catalyst

via a hard-template approach for fuel cell application was also proposed by Atanassov and co-workers [54]. However, the hard-template approaches suffer from the removal of silica using hazardous reagents such as NaOH and HF, and more environmentally friendly approaches are desired. In this context, Hayakawa and co-workers adopted a soft-template approach to obtain mesoporous Fe/N/C catalysts. Figure 11 shows the schematic of the fabrication of N-doped mesoporous carbon via block copolymer-template carbonization of a nitrogen-containing polymer [55–57]. In this method, oligo amic acid, resol, and Pluronic F127 (PEO-PPO-PE triblock copolymer) were used as the N/C source, cross-liner, and soft-template, respectively. The nitrogen-containing aromatic molecules contributed to a high carbonization yield. In the meantime, the soft template could shrink together with other C and N sources and this also contributed to the increase in density of the resulting carbon. In contrast, hard templates such as mesoporous silica do not shrink and result in fragile carbons [2].

After fabricating the mesoporous carbon in the manner illustrated in Figure 11, Fe additive was introduced by impregnation, and the Fe-containing mesoporous carbon was activated under NH_3 at 800 and 1000 °C following the procedure shown in Figure 12. The resulting carbon possessed uniform and periodical mesopores in each particle, as shown in Figure 13. The peak pore size was determined as 4.8 nm and the BET surface area was $1660 \text{ m}^2 \text{ g}^{-1}$. Figure 14 shows the RRDE voltammograms for ORR with the mesoporous Fe/N/C catalyst and a Fe/N/C catalyst prepared without the template. Both catalysts showed fairly good ORR catalytic activity and the voltammograms at the onset region corresponded to each other. In contrast, the diffusion limiting current of the mesoporous catalyst was much better than the catalyst prepared without the template. This result suggests that the mesoporous structure contributed to oxygen diffusion in the catalyst layer. Further studies including MEA testing and optimization of the fabrication method need to be performed to maximize the catalytic activity of such mesoporous Fe/N/C catalysts.

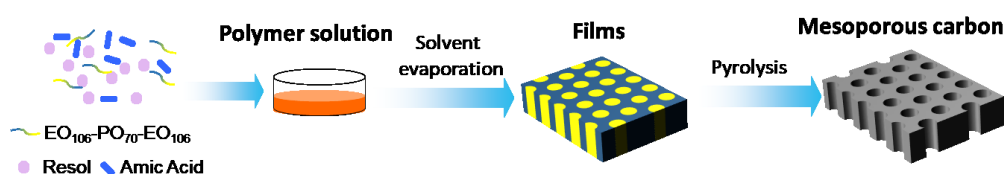


Figure 11. Schematic of the fabrication of mesoporous carbon via block copolymer-templated carbonization.

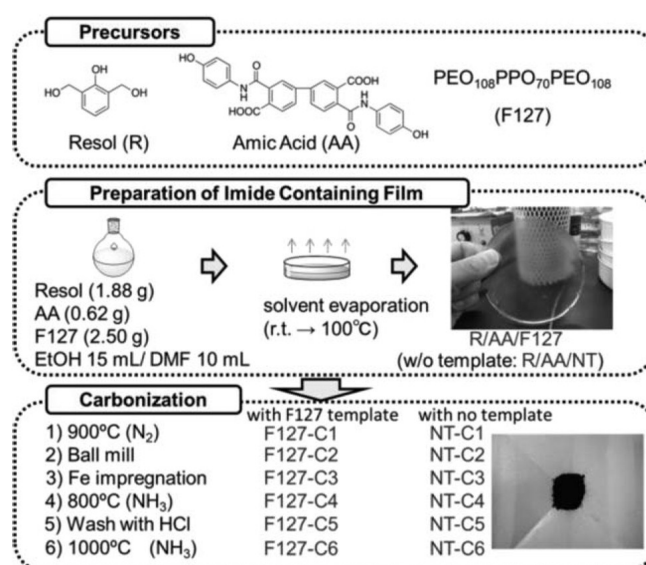


Figure 12. Schematic of the preparation of mesoporous Fe/N/C catalysts [56].

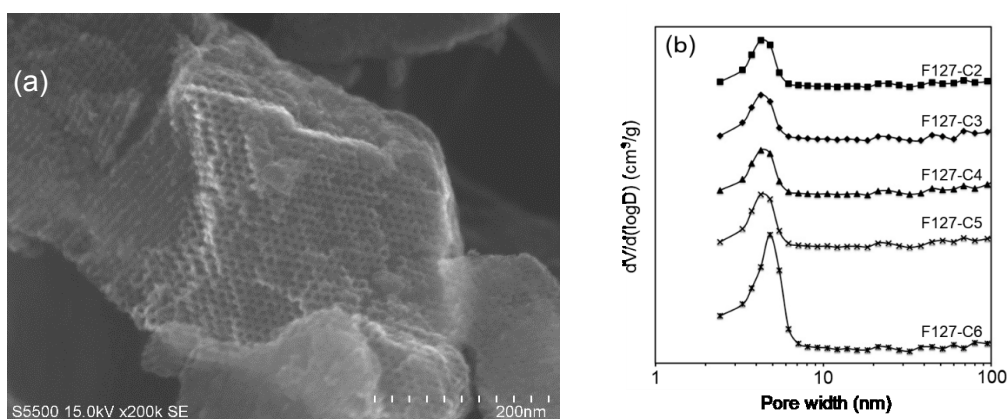


Figure 13. (a) FE-SEM image and (b) pore size distribution of mesoporous Fe/N/C catalyst [56].

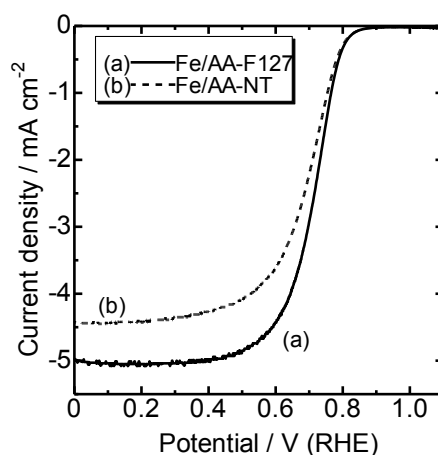


Figure 14. Comparison of the ORR performances at room temperature between catalysts prepared by copolymer-template carbonization and those prepared without using a template [56]. Catalyst loading: 0.2 mg cm^{-2} , electrolyte: O_2 saturated $0.5 \text{ M H}_2\text{SO}_4$, rotation: 1600 rpm.

6. Conclusions

The syntheses and catalytic performances of morphology-controlled Fe/N/C catalysts as NPM oxygen reduction catalysts have been demonstrated. Spherical polyimide nanoparticles synthesized via precipitation polymerization were converted to very active ORR catalysts by multi-step pyrolysis. Mesoporous Fe/N/C catalysts could also be synthesized from nitrogen-containing polymers by block copolymer-templated carbonization. In both cases, the high thermal stability of the nitrogen-containing polymers contributed to control over the morphology of the resulting carbonaceous catalysts. While the ORR performances of Fe/N/C catalysts have improved drastically, ensuring a well-controlled morphology is more important to guarantee sufficient mass transport in the catalyst layer. Building up the desired morphology from infusible nitrogen-containing polymers is beneficial in terms of green chemistry as compared to typical morphological control with inorganic hard templates since it does not suffer from the removal of the template. In addition, further enriched catalytically active sites can be formed while the chemical structures of the precursor polymers can be synthetically optimized. Further studies to improve the catalytic activity and to clarify the detailed reaction mechanism will be conducted in the near future.

Funding: A majority of the studies discussed in this article were funded by the New Energy and Industrial Technology Development Organization (NEDO).

Acknowledgments: The author thanks Toshiba Fuel Cell Poser Systems Co. and Prof Yuji Wada (Tokyo Institute of Technology) for the assistances in fuel cell testing and FE-SEM studies, respectively.

Conflicts of Interest: The authors declare no conflict of interest.

References

1. Yamanaka, I.; Onizawa, T.; Takenaka, S.; Otsuka, K. Direct and continuous production of hydrogen peroxide with 93% selectivity using a fuel-cell system. *Angew. Chemie Int. Ed.* **2003**, *42*, 3653–3655. [[CrossRef](#)] [[PubMed](#)]
2. Park, J.; Nabaee, Y.; Hayakawa, T.; Kakimoto, M. Highly Selective Two-Electron Oxygen Reduction Catalyzed by Mesoporous Nitrogen-Doped Carbon. *ACS Catal.* **2014**, *4*, 3749–3754. [[CrossRef](#)]
3. Fellingner, T.-P.; Hasché, F.; Strasser, P.; Antonietti, M. Mesoporous Nitrogen Doped Carbon for the Electrocatalytic Synthesis of Hydrogen Peroxide. *J. Am. Chem. Soc.* **2012**, *2–4*. [[CrossRef](#)] [[PubMed](#)]
4. Doi, S.; Ishihara, A.; Mitsushima, S.; Kamiya, N.; Ota, K. Zirconium-Based Compounds for Cathode of Polymer Electrolyte Fuel Cell. *J. Electrochem. Soc.* **2007**, *154*, B362. [[CrossRef](#)]
5. Ishihara, A.; Tamura, M.; Ohgi, Y.; Matsumoto, M.; Matsuzawa, K.; Mitsushima, S.; Imai, H.; Ota, K. Emergence of Oxygen Reduction Activity in Partially Oxidized Tantalum Carbonitrides: Roles of Deposited Carbon for Oxygen-Reduction-Reaction-Site Creation and Surface Electron Conduction. *J. Phys. Chem. C* **2013**, *117*, 18837–18844. [[CrossRef](#)]
6. Chisaka, M.; Ando, Y.; Yamamoto, Y.; Itagaki, N. A Carbon-Support-Free Titanium Oxynitride Catalyst for Proton Exchange Membrane Fuel Cell Cathodes. *Electrochim. Acta* **2016**, *214*, 165–172. [[CrossRef](#)]
7. Jasinski, R. A New Fuel Cell Cathode Catalyst. *Nature* **1964**, *201*, 1212–1213. [[CrossRef](#)]
8. Masa, J.; Ozoemena, K. I.; Schuhmann, W.; Zagal, J.H. Fundamental Studies on the Electrocatalytic Properties of Metal Macrocyclics and Other Complexes for the Electroreduction of O₂. In *Electrocatalysis in Fuel Cells*; Springer: London, UK, 2013; pp. 157–212.
9. Jahnke, H.; Schönborn, M.; Zimmermann, G. Organic dyestuffs as catalysts for fuel cells. In *Physical and Chemical Applications of Dyestuffs*; Springer: Berlin/Heidelberg, Germany, 1976; Volume 61, pp. 133–181. ISBN 0340-1022.
10. Dodelet, J.-P. The Controversial Role of the Metal in Fe- or Co-Based Electrocatalysts for the Oxygen Reduction Reaction in Acid Medium. In *Electrocatalysis in Fuel Cells*; Springer: London, UK, 2013; pp. 271–338.
11. Elbaz, L.; Wu, G.; Zelenay, P. Heat-Treated Non-precious-Metal-Based Catalysts for Oxygen Reduction. In *Electrocatalysis in Fuel Cells*; Springer: London, UK, 2013; pp. 213–246.
12. Lefvre, M.; Dodelet, J.P.; Bertrand, P.; Lefe, M. Molecular Oxygen Reduction in PEM Fuel Cells: Evidence for the Simultaneous Presence of Two Active Sites in Fe-Based Catalysts. *J. Phys. Chem. B* **2002**, *106*, 8705–8713. [[CrossRef](#)]
13. Chung, H.T.; Cullen, D.A.; Higgins, D.; Sneed, B.T.; Holby, E.F.; More, K.L.; Zelenay, P. Direct atomic-level insight into the active sites of a high-performance PGM-free ORR catalyst. *Science* **2017**, *357*, 479–484. [[CrossRef](#)] [[PubMed](#)]
14. Wu, J.; Nabaee, Y.; Muthukrishnan, A.; Ohsaka, T. Electrochemical deposition and dissolution of Fe species for N-doped carbon to understand the degradation mechanism of Pt-free oxygen reduction catalysts. *Electrochim. Acta* **2016**, *214*, 307–312. [[CrossRef](#)]
15. Guo, D.; Shibuya, R.; Akiba, C.; Saji, S.; Kondo, T.; Nakamura, J. Active sites of nitrogen-doped carbon materials for oxygen reduction reaction clarified using model catalysts. *Science* **2016**, *351*, 361–365. [[CrossRef](#)] [[PubMed](#)]
16. Wang, X.; Lee, J.S.; Zhu, Q.; Liu, J.; Wang, Y.; Dai, S. Ammonia-treated ordered mesoporous carbons as catalytic materials for oxygen reduction reaction. *Chem. Mater.* **2010**, *22*, 2178–2180. [[CrossRef](#)]
17. Yu, D.; Zhang, Q.; Dai, L. Highly Efficient Metal-Free Growth of Nitrogen-Doped Single-Walled Carbon Nanotubes on Plasma-Etched Substrates for Oxygen Reduction. *J. Am. Chem. Soc.* **2010**, *132*, 15127–15129. [[CrossRef](#)] [[PubMed](#)]

18. Sidik, R.A.; Anderson, A.B.; Subramanian, N.P.; Kumaraguru, S.P.; Popov, B.N. O₂ reduction on graphite and nitrogen-doped graphite: Experiment and theory. *J. Phys. Chem. B* **2006**, *110*, 1787–1793. [[CrossRef](#)] [[PubMed](#)]
19. Ikeda, T.; Boero, M.; Huang, S.F.; Terakura, K.; Oshima, M.; Ozaki, J.I. Carbon alloy catalysts: Active sites for oxygen reduction reaction. *J. Phys. Chem. C* **2008**, *112*, 14706–14709. [[CrossRef](#)]
20. Ikeda, T.; Hou, Z.; Chai, G.L.; Terakura, K. Possible oxygen reduction reactions for graphene edges from first principles. *J. Phys. Chem. C* **2014**, *118*, 17616–17625. [[CrossRef](#)]
21. Damjanovic, A. Distinction between Intermediates Produced in Main and Side Electrode Reactions. *J. Chem. Phys.* **1966**, *45*, 4057. [[CrossRef](#)]
22. Nallathambi, V.; Lee, J.-W.; Kumaraguru, S.P.; Wu, G.; Popov, B.N. Development of high performance carbon composite catalyst for oxygen reduction reaction in PEM Proton Exchange Membrane fuel cells. *J. Power Sources* **2008**, *183*, 34–42. [[CrossRef](#)]
23. Serov, A.; Artyushkova, K.; Atanassov, P. Fe-N-C Oxygen Reduction Fuel Cell Catalyst Derived from Carbendazim: Synthesis, Structure, and Reactivity. *Adv. Energy Mater.* **2014**, *4*, 1301735. [[CrossRef](#)]
24. Iwazaki, T.; Obinata, R.; Sugimoto, W.; Takasu, Y. High oxygen-reduction activity of silk-derived activated carbon. *Electrochem. Commun.* **2009**, *11*, 376–378. [[CrossRef](#)]
25. Olson, T.S.; Pylypenko, S.; Fulghum, J.E.; Atanassov, P. Bifunctional Oxygen Reduction Reaction Mechanism on Non-Platinum Catalysts Derived from Pyrolyzed Porphyrins. *J. Electrochem. Soc.* **2010**, *157*, B54. [[CrossRef](#)]
26. Hsueh, K.L.; Chin, D.T.; Srinivasan, S. Electrode kinetics of oxygen reduction. A theoretical and experimental analysis of the rotating ring-disc electrode method. *J. Electroanal. Chem.* **1983**, *153*, 79–95. [[CrossRef](#)]
27. Muthukrishnan, A.; Nabae, Y.; Hayakawa, T.; Okajima, T.; Ohsaka, T. Fe-containing polyimide-based high-performance ORR catalysts in acidic medium: A kinetic approach to study the durability of catalysts. *Catal. Sci. Technol.* **2015**, *5*, 475–483. [[CrossRef](#)]
28. Muthukrishnan, A.; Nabae, Y.; Okajima, T.; Ohsaka, T. Kinetic Approach to Investigate the Mechanistic Pathways of Oxygen Reduction Reaction on Fe-Containing N-Doped Carbon Catalysts. *ACS Catal.* **2015**, *5*. [[CrossRef](#)]
29. Muthukrishnan, A.; Nabae, Y. Estimation of the inherent kinetic parameters for oxygen reduction over a Pt-free cathode catalyst by resolving the quasi-four-electron reduction. *J. Phys. Chem. C* **2016**, *120*, 22515–22525. [[CrossRef](#)]
30. van Veen, J.A.R.; Colijn, H.A.; van Baar, J.F. On the effect of a heat treatment on the structure of carbon-supported metalloporphyrins and phthalocyanines. *Electrochim. Acta* **1988**, *33*, 801–804. [[CrossRef](#)]
31. Gojkovic, S.L.; Gupta, S.; Savinell, R.F. Heat-Treated Iron(III) Tetramethoxyphenyl Porphyrin Supported on High-Area Carbon as an Electrocatalyst for Oxygen Reduction. *J. Electrochem. Soc.* **1998**, *145*, 3493. [[CrossRef](#)]
32. Yeager, E. Electrocatalysts for O₂ reduction. *Electrochim. Acta* **1984**, *29*, 1527–1537. [[CrossRef](#)]
33. Bron, M.; Radnik, J.; Fieber-Erdmann, M.; Bogdanoff, P.; Fiechter, S. EXAFS, XPS and electrochemical studies on oxygen reduction catalysts obtained by heat treatment of iron phenanthroline complexes supported on high surface area carbon black. *J. Electroanal. Chem.* **2002**, *535*, 113–119. [[CrossRef](#)]
34. Lalande, G.; Coté, R.; Guay, D.; Dodelet, J.P.; Weng, L.T.; Bertrand, P. Is nitrogen important in the formulation of Fe-based catalysts for oxygen reduction in solid. *Electrochim. Acta* **1997**, *42*, 1379–1388. [[CrossRef](#)]
35. Herranz, J.; Lefèvre, M.; Larouche, N.; Stansfield, B.; Dodelet, J.P. Step-by-step synthesis of non-noble metal electrocatalysts for O₂ reduction under proton exchange membrane fuel cell conditions. *J. Phys. Chem. C* **2007**, *111*, 19033–19042. [[CrossRef](#)]
36. Alves, M.C.M.; Dodelet, J.P.; Guay, D.; Ladouceur, M.; Tourillon, G. Origin of the electrocatalytic properties for oxygen reduction of some heat-treated polyacrylonitrile and phthalocyanine cobalt compounds adsorbed on carbon black as probed by electrochemistry and x-ray absorption spectroscopy. *J. Phys. Chem.* **1992**, *96*, 10898–10905. [[CrossRef](#)]
37. Chokai, M.; Taniguchi, M.; Moriya, S.; Matsubayashi, K.; Shinoda, T.; Nabae, Y.; Kuroki, S.; Hayakawa, T.; Kakimoto, M.; Ozaki, J.-I.; et al. Preparation of carbon alloy catalysts for polymer electrolyte fuel cells from nitrogen-containing rigid-rod polymers. *J. Power Sources* **2010**, *195*, 5947–5951. [[CrossRef](#)]
38. Wu, G.; More, K.L.; Johnston, C.M.; Zelenay, P. High-performance electrocatalysts for oxygen reduction derived from polyaniline, iron, and cobalt. *Science* **2011**, *332*, 443–447. [[CrossRef](#)] [[PubMed](#)]

39. Wood, T.E.; Tan, Z.; Schmoeckel, A.K.; O'Neill, D.; Atanasoski, R. Non-precious metal oxygen reduction catalyst for PEM fuel cells based on nitroaniline precursor. *J. Power Sources* **2008**, *178*, 510–516. [[CrossRef](#)]
40. Asao, K. Preparation and Application of Polyimide Particles. *J. Photopolym. Sci. Technol.* **2014**, *27*, 181–185. [[CrossRef](#)]
41. Sawai, T.; Uchida, T.; Yamazaki, S.; Kimura, K. Preparation of Novel Naphthalene Polyimide and Its Morphology. *J. Photopolym. Sci. Technol.* **2013**, *26*, 341–344. [[CrossRef](#)]
42. Sawai, T.; Wakabayashi, K.; Yamazaki, S.; Uchida, T.; Sakaguchi, Y.; Yamane, R.; Kimura, K. Synthesis and morphology control of self-condensable naphthalene-containing polyimide by using reaction-induced crystallization. *Eur. Polym. J.* **2013**, *49*, 2334–2343. [[CrossRef](#)]
43. Chokai, M.; Nabae, Y.; Kuroki, S.; Hayakawa, T.; Kakimoto, M.; Miyata, S. Preparation of Carbon-Based Catalysts for PEFC from Nitrogen-Containing Aromatic Polymers. *J. Photopolym. Sci. Technol.* **2011**, *24*, 241–246. [[CrossRef](#)]
44. Nabae, Y.; Kuang, Y.; Chokai, M.; Ichihara, T.; Isoda, A.; Hayakawa, T.; Aoki, T. High performance Pt-free cathode catalysts for polymer electrolyte membrane fuel cells prepared from widely available chemicals. *J. Mater. Chem. A* **2014**, *2*, 11561–11564. [[CrossRef](#)]
45. Nabae, Y.; Nagata, S.; Hayakawa, T.; Niwa, H.; Harada, Y.; Oshima, M.; Isoda, A.; Matsunaga, A.; Tanaka, K.; Aoki, T. Pt-free carbon-based fuel cell catalyst prepared from spherical polyimide for enhanced oxygen diffusion. *Sci. Rep.* **2016**, *6*, 23276. [[CrossRef](#)] [[PubMed](#)]
46. Nabae, Y.; Nagata, S. Oxygen Reduction Catalytic Activity of Carbon-based Cathode Catalyst Prepared from Polyimide Nano-Particles Containing Fe-Phenanthroline Complex. *J. Photopolym. Sci. Technol.* **2016**, *29*, 255–258. [[CrossRef](#)]
47. Nabae, Y.; Sonoda, M.; Yamauchi, C.; Hosaka, Y.; Isoda, A.; Aoki, T. Highly durable Pt-free fuel cell catalysts prepared by multi-step pyrolysis of Fe phthalocyanine and phenolic resin. *Catal. Sci. Technol.* **2014**, *4*, 1400. [[CrossRef](#)]
48. Proietti, E.; Jaouen, F.; Lefèvre, M.; Larouche, N.; Tian, J.; Herranz, J.; Dodelet, J.-P. Iron-based cathode catalyst with enhanced power density in polymer electrolyte membrane fuel cells. *Nat. Commun.* **2011**, *2*, 416. [[CrossRef](#)] [[PubMed](#)]
49. Strickland, K.; Miner, E.; Jia, Q.; Tylus, U.; Ramaswamy, N.; Liang, W.; Sougrati, M.; Jaouen, F.; Mukerjee, S. Highly active oxygen reduction non-platinum group metal electrocatalyst without direct metal–nitrogen coordination. *Nat. Commun.* **2015**, *6*, 7343. [[CrossRef](#)] [[PubMed](#)]
50. Banham, D.; Kishimoto, T.; Zhou, Y.; Sato, T.; Bai, K.; Ozaki, J.; Imashiro, Y.; Ye, S. Critical advancements in achieving high power and stable nonprecious metal catalyst-based MEAs for real-world proton exchange membrane fuel cell applications. *Sci. Adv.* **2018**, *4*, 1–7. [[CrossRef](#)] [[PubMed](#)]
51. Vinu, A.; Ariga, K.; Mori, T.; Nakanishi, T.; Hishita, S.; Golberg, D.; Bando, Y. Preparation and characterization of well-ordered hexagonal mesoporous carbon nitride. *Adv. Mater.* **2005**, *17*, 1648–1652. [[CrossRef](#)]
52. Park, S.S.; Chu, S.-W.; Xue, C.; Zhao, D.; Ha, C.-S. Facile synthesis of mesoporous carbon nitrides using the incipient wetness method and the application as hydrogen adsorbent. *J. Mater. Chem.* **2011**, *21*, 10801. [[CrossRef](#)]
53. Fulvio, P.F.; Jaroniec, M.; Liang, C.; Dai, S. Polypyrrole-based nitrogen-doped carbon replicas of SBA-15 and SBA-16 containing magnetic nanoparticles. *J. Phys. Chem. C* **2008**, *112*, 13126–13133. [[CrossRef](#)]
54. Carroll, N.J.; Pylypenko, S.; Atanassov, P.B.; Petsev, D.N. Microparticles with bimodal nanoporosity derived by microemulsion templating. *Langmuir* **2009**, *25*, 13540–13544. [[CrossRef](#)] [[PubMed](#)]
55. Liu, Y.; Ohnishi, K.; Sugimoto, S.; Okuhara, K.; Maeda, R.; Nabae, Y.; Kakimoto, M.; Wang, X.; Hayakawa, T. Well-ordered mesoporous polymers and carbons based on imide-incorporated soft materials. *Polym. Chem.* **2014**, *5*, 6452–6460. [[CrossRef](#)]

56. Nabae, Y.; Nagata, S.; Ohnishi, K.; Liu, Y.; Sheng, L.; Wang, X.; Hayakawa, T. Block copolymer templated carbonization of nitrogen containing polymer to create fine and mesoporous carbon for oxygen reduction catalyst. *J. Polym. Sci. Part A Polym. Chem.* **2017**, *55*, 464–470. [[CrossRef](#)]
57. Gao, L.; Chandra, A.; Nabae, Y.; Hayakawa, T. Inducing defects in ordered mesoporous carbons via the block copolymer-templated high-temperature carbonization of nitrogen-containing polymeric precursors. *Polym. J.* **2018**. [[CrossRef](#)]



© 2018 by the author. Licensee MDPI, Basel, Switzerland. This article is an open access article distributed under the terms and conditions of the Creative Commons Attribution (CC BY) license (<http://creativecommons.org/licenses/by/4.0/>).